Check for updates

Geophysical Research Letters

RESEARCH LETTER
10.1029/2022GL100841

Relativistic Microburst Scale Size Induced by a Single Point-Source Chorus Element

Ning Kang[1], Jacob Bortnik[1], Xiaojia Zhang[2], Seth Claudepierre[1], and Xiaofei Shi[2]

[1]Department of Atmospheric and Oceanic Sciences, University of California Los Angeles, Los Angeles, CA, USA, [2]Department of Earth, Planetary, and Space Sciences, University of California Los Angeles, Los Angeles, CA, USA

Key Points:

- We use an event-based model with propagation in an inhomogeneous magnetosphere to study chorus-induced relativistic microburst scale size
- A primary precipitation burst is seen near the wave source field line by resonance with quasi-parallel waves near equatorial source region
- A secondary precipitation burst is seen on more poleward L-shell by resonance with high latitude oblique waves with scale size 20–40 km

Supporting Information:

Supporting Information may be found in the online version of this article.

Correspondence to:

N. Kang,
nkang20@atmos.ucla.edu

Citation:

Kang, N., Bortnik, J., Zhang, X., Claudepierre, S., & Shi, X. (2022). Relativistic microburst scale size induced by a single point-source chorus element. *Geophysical Research Letters*, *49*, e2022GL100841. https://doi.org/10.1029/2022GL100841

Received 14 AUG 2022
Accepted 1 DEC 2022

Author Contributions:

Data curation: Xiaojia Zhang, Xiaofei Shi
Formal analysis: Xiaojia Zhang, Seth Claudepierre, Xiaofei Shi
Funding acquisition: Seth Claudepierre

© 2022. The Authors.
This is an open access article under the terms of the Creative Commons Attribution-NonCommercial-NoDerivs License, which permits use and distribution in any medium, provided the original work is properly cited, the use is non-commercial and no modifications or adaptations are made.

Abstract Relativistic microbursts are impulsive, sub-second precipitation bursts of relativistic electrons. They are one of the main loss mechanisms of outer radiation belt electrons, and are driven by chorus waves. The scale size of relativistic microbursts is still not fully understood. In this work a global modeling of the microburst spatial distribution is conducted to study the scale size of relativistic microburst induced by chorus waves. A primary precipitation burst is induced near the source region by quasi-parallel waves, and a secondary precipitation (SP) is induced on higher L-shells by further-propagating, oblique waves. The SP has a significant scale size even with a point-source assumption because of wave spreading due to propagation effect. The secondary relativistic microburst scale size is ∼40(20) km on the counter (co)-streaming side, consistent with previous observations. Our modeling results indicate chorus wave propagation effects are one of the primary factors controlling the relativistic microburst scale size.

Plain Language Summary Relativistic microbursts are impulsive relativistic electron precipitation events from the radiation belt into atmosphere, occurring within 1 s. They are an important mechanism that can empty the outer radiation belt, and are driven by one kind of commonly observed electromagnetic wave in magnetosphere called chorus waves. The factors controlling the scale size of relativistic microbursts is still not fully understood. This work model the spatial distribution of microbursts on the ground, from which the scale size of relativistic microbursts can be inferred. Two kinds of relativistic microbursts are observed in the simulation, one called primary precipitation occurs near wave source region, the other called secondary precipitation (SP) occurs at higher L shells. The SP scale size is ∼40 km on southern hemisphere and ∼20 km on northern hemisphere, consistent with previous observations. Our modeling results also indicate that there could be a spatial distribution of microburst not only because the chorus wave source has a finite length but because chorus waves diverge in space after propagating away from the source location.

1. Introduction

Microbursts are an impulsive electron precipitation burst with a time scale of less than 1 s. They are observed over a wide range of energies, from several tens of keV (Anderson & Milton, 1964; Miyoshi et al., 2015) up to multiple MeV (Douma et al., 2017; Imhof et al., 1992; Lorentzen, Looper, et al., 2001). Many studies link the several tens to hundreds keV microbursts with the pulsating aurora (Hofmann & Greene, 1972; Kawamura et al., 2021; Miyoshi et al., 2015; Sandahl et al., 1980; Shumko et al., 2021). Microbursts are also crucial for the chemical composition of the upper atmosphere (Marshall & Bortnik, 2018; Miyoshi et al., 2021). Relativistic electron (>1 MeV) microbursts are one of the important loss mechanisms for outer radiation belt relativistic electrons (Douma et al., 2019; Lorentzen, Blake, et al., 2001; O'Brien et al., 2004; Thorne et al., 2005).

Microbursts are believed to be closely related to chorus waves. Microbursts are often observed as a series of grouped events with a spacing <1 s and a total duration of $\sim 10-15$ s (Anderson & Milton, 1964), called microburst trains (Tsurutani et al., 2013). Previous statistical studies (Douma et al., 2017; Nakamura et al., 2000; Zhang et al., 2022) reveal that microbursts have a higher occurrence rate at more disturbed times and are most likely to be observed on the dawn sector between $L = 4 \sim 6$, and these statistical characteristics are consistent with the characteristics of chorus waves (Li et al., 2009; O'Brien et al., 2003). Direct evidence of association between chorus waves and microbursts are also reported (Breneman et al., 2017; Lorentzen, Looper, et al., 2001). Therefore, it is widely accepted that chorus waves scattering energetic electrons into loss cone is one of the most important mechanisms for generating microbursts.

19448007, 2022, 23, Downloaded from https://agupubs.onlinelibrary.wiley.com/doi/10.1029/2022GL100841 by University of California - Los Angeles, Wiley Online Library on [09/10/2023]. See the Terms and Conditions (https://onlinelibrary.wiley.com/terms-and-conditions) on Wiley Online Library for rules of use; OA articles are governed by the applicable Creative Commons License

The scale size of microbursts near the Earth's surface is important for both understanding the impact of microbursts on the atmosphere and estimating the total energetic electron loss from the outer radiation belt, but this remains an open question due to the difficulty of constraining the scale size from a single spacecraft. Several attempts have been made to measure the microburst scale size: Crew et al. (2016) and Shumko et al. (2018) use simultaneous observation of the same microburst by two spatially separated spacecrafts to estimate the scale size as 11 and 29 km, respectively. Parks (1967) used balloon arrays to obtain a spatial resolution and measures a scale size of 40 ± 14 km. Blake et al. (1996) analyze the condition to observe a bouncing microburst based on the sampling period of SAMPEX spacecraft and give a lower limit of a few tens of km for the scale size. Shumko et al. (2020) apply probabilistic tools to analyze the AeroCube-6 data and derive the most probable range of scale size is $12 \sim 47$ km.

In this work, we model the scale size of a relativistic electron microburst that is produced by a chorus wave element through a 2D global ray tracing modeling. Most previous modeling studies of microbursts (Chen et al., 2020; Hikishima et al., 2010; Miyoshi et al., 2010, 2020; Saito et al., 2012) focus on the particle dynamics on only one field line and usually assume parallel propagating chorus waves only. This assumption makes the analysis unable to recreate a spatial distribution over different L-shells, and furthermore, it is known that a strictly parallel propagating, field line guided chorus waves is relatively uncommon in a smooth, inhomogeneous magnetosphere (Lauben et al., 2002; Santolik et al., 2003). In this work, we use a global precipitation model that takes full account of the propagation effects of chorus waves, therefore the model is able to construct a cross-L-shell wavefield distribution by a single chorus wave source and further a latitudinal distribution of precipitation flux on the ground.

2. Method and Model

The numerical model we use in this work is the same as the one in Kang and Bortnik (2022) and Bortnik et al. (2006a, 2006b), except that the ray tracing setup is adjusted to accommodate an equatorial chorus wave source. The model first performs various ray tracing runs for chorus waves with different frequencies and wave normal angles (WNAs) launched from a single point source, thus constructing the wavefield in space-time. Then a test-particle-like method is conducted on different L-shells to calculate the electron precipitation on different field lines. Technical details of this model are given in Bortnik et al. (2006a) and a brief introduction is given in Supporting Information S1.

We initialize the model based on a chorus wave event observed by RBSP-B. On 8 January 2018, RBSP-B observed lower band chorus waves at around $L = 6$, which lasted for about 1.5 hr. The electric and magnetic field spectrum of this event is shown in Figures 1a and 1b. The wave source location in the ray tracing part is set to be the equator of $L = 6$ accordingly. The wave power during the 1.5-hr event is averaged as a function of different frequency and WNAs, obtained using the "instantaneous frequency" method of Santolik et al. (2014). The results are shown in Figure 1c. We see that the chorus waves are primarily quasi-parallel (mainly between $\pm 20°$) with power peaked at around 0.2 local gyrofrequency (f_{ce}). This statistical result is used as the frequency and WNA distribution for the ray tracing initialization. All waves have an initial wave normal pointing northward so they all propagate northward. The 1.5-hr averaged electron flux from the Energetic particle, Composition, and Thermal plasma suite aboard RBSP-B is shown in Figure 1d. This is used as the trapped flux function in the test-particle part, meanwhile the flux function between 1 and 100 keV is converted to a distribution function for Landau damping calculation in the ray tracing part.

3. Results

3.1. Ray Tracing Results

Figure 2 shows the ray trajectories of three different frequencies, 0.1, 0.3, and 0.5 f_{ce}, marked by blue, green, and red lines, respectively, that are representative of the chorus wave power trajectory. The rays with the same frequency have different trajectories because their initial WNAs are different. For the sake of a clear illustration, the ray trajectories are truncated at a latitude of 40° (unless the rays are already damped out below 40° according to the Landau damping calculation in the ray tracing part, in which case the rays are also truncated), but actually many rays propagate beyond 40°, and some even experience a bouncing at higher latitude (see Figure 1

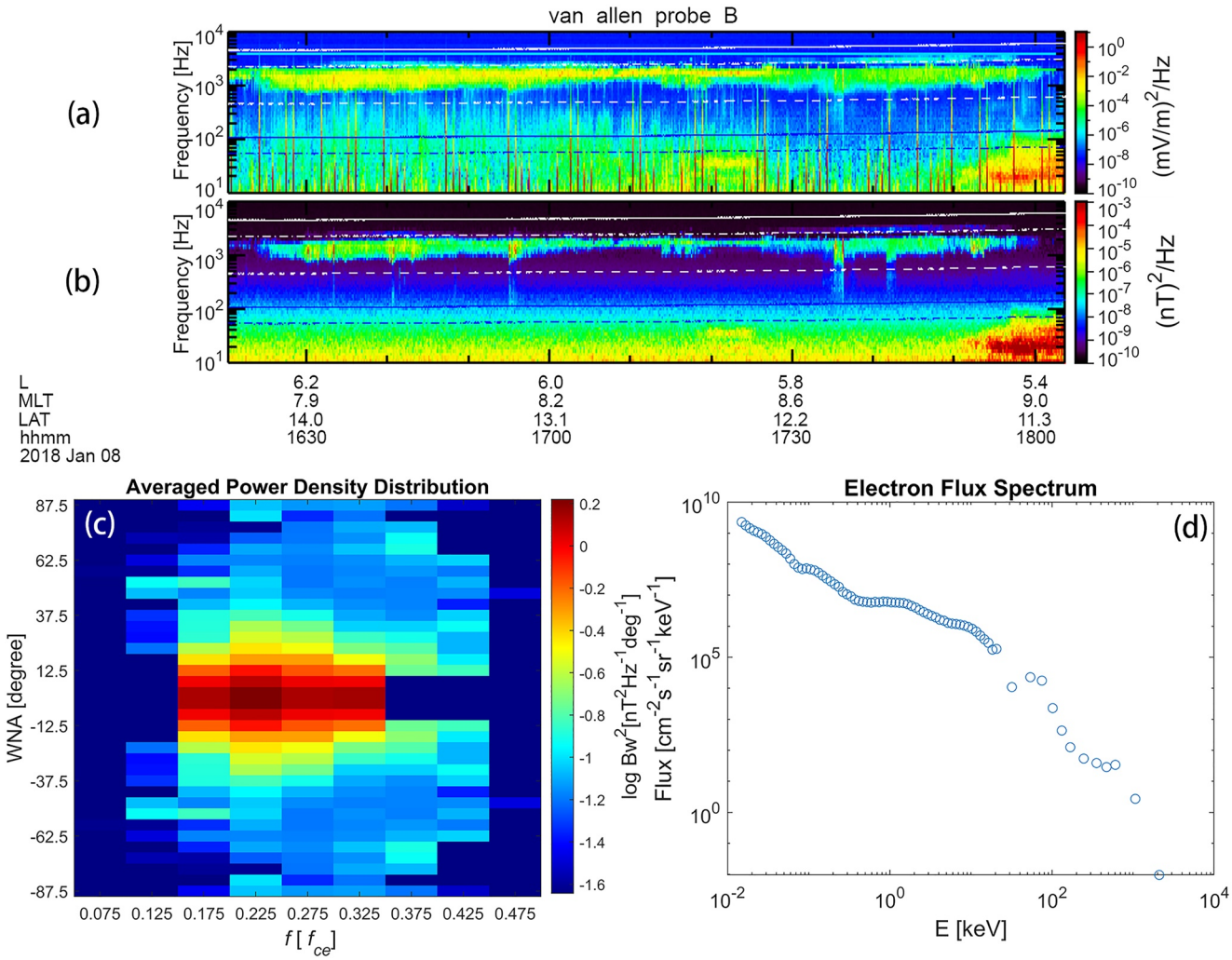

Figure 1. Overview of the chorus event used for the modeling setup. (a) Electric field and (b) magnetic field components of the chorus wave event observed by the EMFISIS instrument on RBSP-B for a ~1.5 hr period on 8 January 2018. The white dashed lines, dot-dashed lines, and solid lines in both panels correspond to 0.1 f_{ce}, 0.5 f_{ce} and 1.0, respectively. (c) The statistical lower band wave power density as a function of frequency and wave normal angle, obtained by averaging all the wave power of chorus elements over the entire 1.5-hr event. (d) The 1.5-hr-averaged electron flux energy spectrum near the loss cone during the event observed by RBSP-B.

in Supporting Information S1 for some examples), which will be mentioned later. Several points that would be important to the discussion later should be made from these results.

First, even though the chorus wave source region is assumed to be a single point here, the waves are still able to cover a wide range of L-shells, which produces a spatial distribution of precipitation flux on the ground. This is because there are different frequency modes and different initial WNAs in the chorus wave element, therefore their propagation behavior will also be different. Another interesting point is that although the wave trajectories diverge to L-shells both lower and higher than $L = 6$, most wave power actually propagates to higher L-shells. This can be seen by roughly counting the number of rays on both sides of the $L = 6$ field line. Some final minor points about the ray tracing result are that chorus waves with higher frequency tend to experience heavier damping according to the Landau damping calculation based on the observed electron distribution (therefore get terminated quicker within shorter distance) and have more converged ray trajectories. This frequency dependence may indicate lower frequency chorus waves produce a microburst with higher flux and larger scale size but this trend needs further investigation to confirm.

19448007, 2022, 23, Downloaded from https://agupubs.onlinelibrary.wiley.com/doi/10.1029/2022GL100841 by University of California - Los Angeles, Wiley Online Library on [09/10/2023]. See the Terms and Conditions (https://onlinelibrary.wiley.com/terms-and-conditions) on Wiley Online Library for rules of use; OA articles are governed by the applicable Creative Commons License

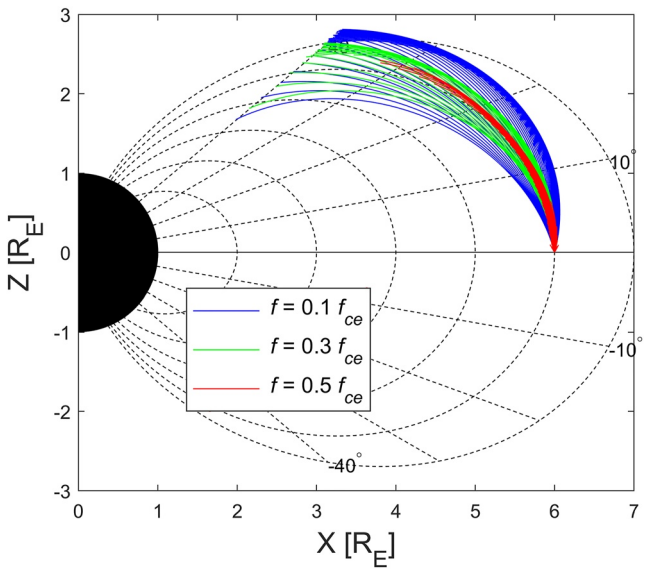

Figure 2. A selected portion of a few representative example ray paths in the ray tracing model. The blue, green and red solid lines are rays have frequencies of 0.1 f_{ce}, 0.3 f_{ce}, and 0.5 f_{ce}, respectively. Rays with each frequency have different initial wave normal angles ranging from −60° to 60°.

3.2. Precipitation Flux Spectrum on a Single L-Shell

Before examining the spatial distribution of the relativistic microburst over multiple L-shells, we first focus on the precipitation flux signature on both the L-shell of the wave source $L = 6$ and at a higher L-shell $L = 6.664$. Figure 3 shows the precipitation flux spectra seen at both the northern and southern foot points of these two field lines. The x-axis is the time span of 2 s, where $t = 0$ is the time the chorus waves are launched from the source location, and the y-axis is the energy of precipitated electrons.

We mainly focus on the field line at $L = 6.664$, whose spectra seen on northern and southern hemisphere are Figures 3a and 3b, respectively. We address a very important point that all the precipitations occurring on this field line are due to chorus waves that have propagated to high latitudes and turned oblique, as indicated in Figure 2. Clear relativistic precipitation near 1 MeV energies (white horizontal dashed line) is observed in both hemispheres (feature labeled (i) in both panels). Because the waves propagate northward, the precipitated electrons in the southern hemisphere are counter-streaming with the waves, and therefore are scattered due to first order cyclotron resonance with chorus waves, whilst the precipitated electrons on northern hemisphere are co-streaming and scatter due to anomalous cyclotron resonance. The precipitation flux in the southern hemisphere is several times higher than the northern hemisphere, as would be expected since cyclotron resonance is stronger than anomalous cyclotron resonance. The duration of part (i) is about 0.2 s, which is a typical timescale for a microburst.

A much weaker precipitation signature also around the 1 MeV energy range and lagging behind part (i) by about 0.2 s (feature labeled (ii) in both panels) is observed on both hemispheres. These parts are induced by the magnetospherically reflected, equatorward traveling chorus waves we mentioned in Section 3.1. Those waves are already highly damped after traveling to a very high latitude and experiencing a magnetospheric reflection, therefore the induced precipitation flux is also much weaker. Part (ii) is four orders of magnitude weaker than part (i), which suggests their contribution is negligible for overall radiation belt loss and may not generally be reflected in microburst observations.

Apart from the relativistic precipitation parts, there is also a very significant sub-relativistic ($\sim 1 - 100$ keV) precipitation signature in the northern hemisphere (feature (iii) in panel (a)). Considering the energy range and the co-streaming nature of this part of electrons, this feature of the precipitation is due to Landau resonance with the chorus waves. This is consistent with recent studies showing that Landau resonance with oblique chorus waves can induce intense sub-relativistic microburst precipitation (Artemyev et al., 2022). Note that such strong sub-relativistic precipitation is not seen in the southern hemisphere because of the co-streaming nature of Landau resonance, which, in this case would only show up in the northern hemisphere, whereas the southern hemisphere will only exhibit the energetic electron precipitation portion. This may explain why microbursts near 1 MeV and 150 keV are not always correlated (Blake et al., 1996, Figure 10). There exists, however, a part of the sub-relativistic precipitation in the southern hemisphere (part (iii) in panel (b)), but the flux is four orders of magnitude weaker than part (iii) in panel (a) because this part of precipitation is induced by Landau resonance with the magnetospherically reflected, highly damped chorus waves (the co-streaming condition is satisfied because the propagation direction reverses after bouncing).

The overall features of the spectra for the source region $L = 6$ (Figures 3c and 3d for northern and southern hemisphere footpoint, respectively) are the same as discussed earlier for $L = 6.664$. The corresponding features are also labeled i, ii and iii in the plot. The major difference is the energy range. On the wave source field line, electrons resonate with quasi-parallel chorus waves near the equatorial source region, therefore the energy of electrons scattered by (anomalous) cyclotron resonance is mainly in $10\,s \sim 100\,s$ keV range (we remind readers there is anomalous cyclotron resonance in the source region because we introduce a spread in the WNA distribution). Their contribution to the relativistic microburst above 1 MeV is limited to a weak high-energy tail of the spectrum, which is consistent with recent observation studies (Kawamura et al., 2021; Shumko et al., 2021), and the spectrum feature is also consistent with recent modeling works (Miyoshi et al., 2020, Figure 2). In contrast,

19448007, 2022, 23, Downloaded from https://agupubs.onlinelibrary.wiley.com/doi/10.1029/2022GL100841 by University of California - Los Angeles, Wiley Online Library on [09/10/2023]. See the Terms and Conditions (https://onlinelibrary.wiley.com/terms-and-conditions) on Wiley Online Library for rules of use; OA articles are governed by the applicable Creative Commons License

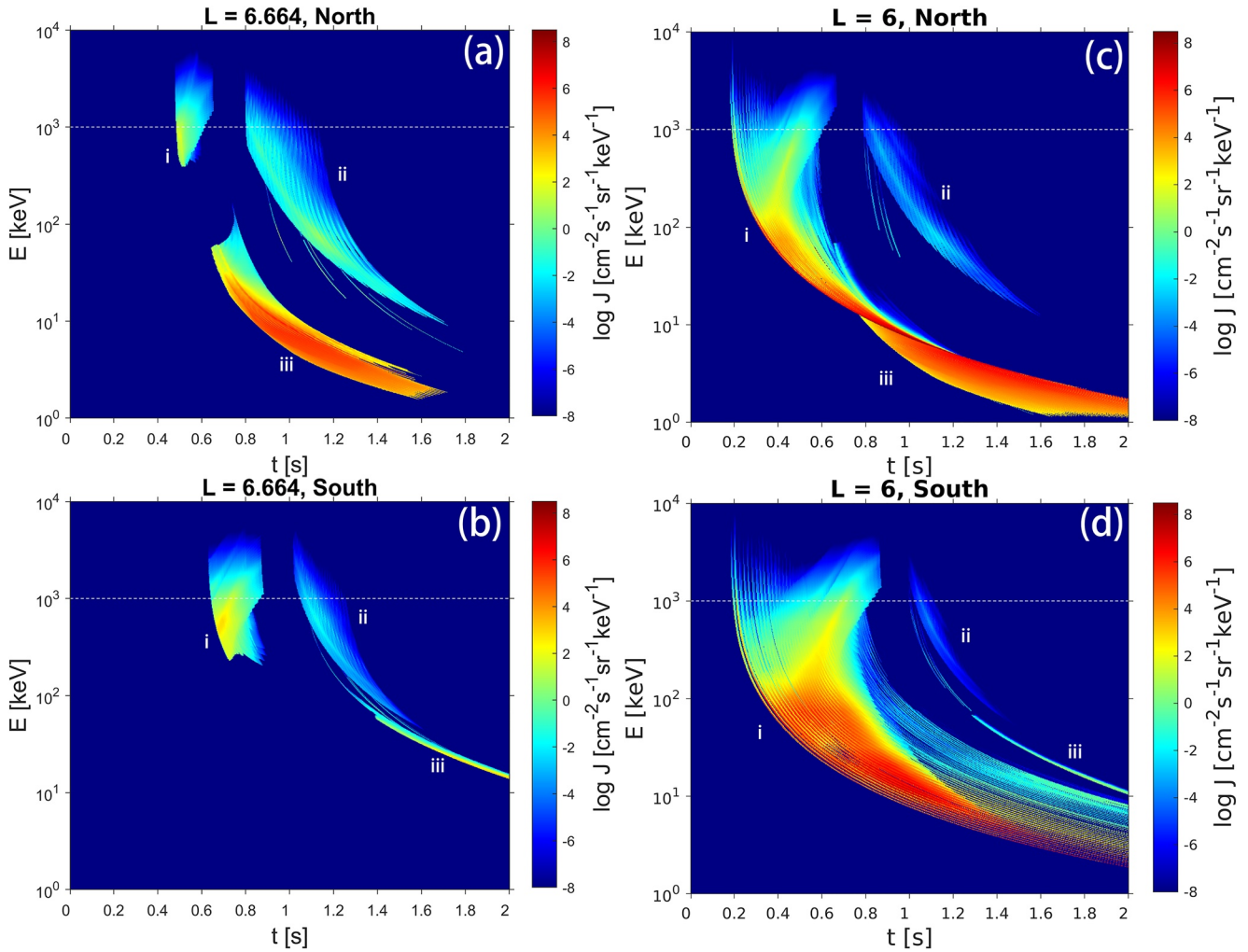

Figure 3. Energy-time spectrum of (a) northern and (b) southern hemisphere precipitation flux on the field line at $L = 6.664$, and (c) northern and (d) southern hemisphere precipitation flux on the field line at $L = 6$. The white dashed line marks 1 MeV energy. Several numbers are added to indicate different parts of the precipitation signature spectra.

the minimum resonance energy with oblique chorus waves on $L = 6.664$ is as high as several keV, therefore their contribution to relativistic microburst is significant even though the waves experience damping after traveling to higher latitudes.

3.3. Spatial Distribution of Relativistic Precipitation and Scale Size

The precipitation flux spectrum for one L-shell is calculated repeatedly for an interval of L-shells between 5.9 and 7.24, which correspond to invariant latitudes between 65.5° and 68°. These flux spectra on different L-shells allow us to construct the latitudinal distribution of the precipitation flux on the ground (which would be very similar to that observed by low-Earth-orbit (LEO) satellites, or by ionospheric sensing methods (Johnson et al., 1999)). To study the scale size of the relativistic microburst, we examine the latitudinal distribution of the integrated total flux above 1 MeV in both the northern and southern hemispheres. The results are plotted in Figure 4. Panels (a) and (d) represent the total flux above 1 MeV in northern and southern hemispheres, respectively. The *x*-axis is the latitude on the ground/corresponding L-shell, and the *y*-axis is the flux. Curves for snapshots taken at different times during the simulation are color coded in the color bar. The black vertical dashed line marks the latitude corresponding to the wave source at $L = 6$. The instantaneous maximum flux values are plotted in the red curve of panel (b) and (e), respectively, corresponding to the right *y*-axis. The location of the instantaneous maximum

19448007, 2022, 23, Downloaded from https://agupubs.onlinelibrary.wiley.com/doi/10.1029/2022GL100841 by University of California - Los Ange, Wiley Online Library on [09/10/2023]. See the Terms and Conditions (https://onlinelibrary.wiley.com/terms-and-conditions) on Wiley Online Library for rules of use; OA articles are governed by the applicable Creative Commons License

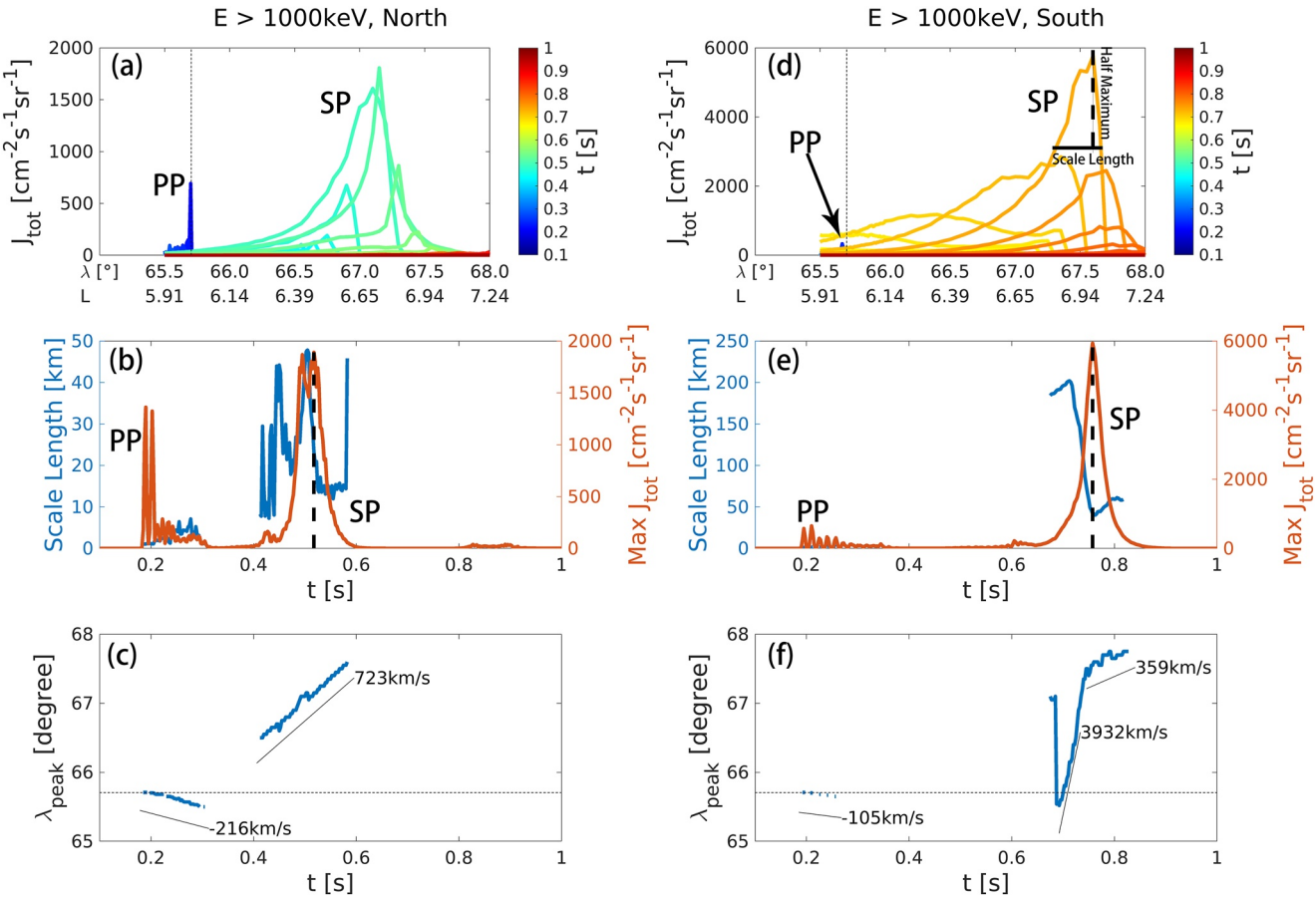

Figure 4. >1 MeV Microburst precipitation flux evolution on the ground surface as a function of latitude and time for (a) northern and (d) southern hemisphere. The black dashed vertical line marks the location of wave source L shell of 6. An illustration of how the scale length is defined is shown in (d). (b and e) show the time evolution of instantaneous maximum flux and scale length for northern and southern hemisphere, respectively. The red lines are the instantaneous maximum fluxes corresponding to the *y* axis on the right, and the blue lines are the scale lengths corresponding to the *y* axis on the left. (c and f) show the time evolution of the location of instantaneous peak fluxes of northern and southern hemisphere, respectively, with reference lines of different velocities. The black dashed horizontal line marks the location of wave source L shell of 6.

flux peak λ_{peak} is shown in panel (c) and (f), respectively. The horizontal black dashed lines also mark the invariant latitude of source L-shell.

One of the most important features to notice is that there are two distinct kinds of precipitation, both in the northern and southern hemispheres. The first kind of precipitation appears between $0.1 \sim 0.2\,s$ near the source L-shell, which is called the PP. The second one appears later at higher L-shells, called the SP. We conclude that the PP is induced by resonance with quasi-parallel chorus waves in the equatorial source region (corresponding to Figures 3c and 3d), by observing that they appear close to the source L-shell, they arise just at the flight time for electrons starting from equator, and they appear simultaneously in both hemispheres. Conversely, the SP is induced by resonance with oblique chorus waves that have already traveled to higher L-shells and higher latitudes (corresponding to Figures 3a and 3b). Due to our assumption of point-source chorus wave, we will focus on the analysis of the SP, while leaving the impact of point-source assumption on PP to the discussion section. Here we only address one major difference, namely that the PP moves equatorward, while SP moves poleward (Panel (a), (c), (d), and (f)), which is a feature that might be valuable for comparison with observations.

Several characteristics of the evolution of the SP can be gleaned from these results. The whole process occurs within a short time of 0.2 s, which is a typical temporal signature of a microburst. The locations of the flux peaks are poleward displaced from the chorus wave source location $L = 6$ (corresponding to an invariant latitude of 65.7°), and the peak keeps moving poleward with time. By tracking the flux peak location, we can estimate that the flux peak moves poleward at an average speed of 354 km/s in the southern hemisphere and 721 km/s

19448007, 2022, 23, Downloaded from https://agupubs.onlinelibrary.wiley.com/doi/10.1029/2022GL100841 by University of California - Los Ange, Wiley Online Library on [09/10/2023]. See the Terms and Conditions (https://onlinelibrary.wiley.com/terms-and-conditions) on Wiley Online Library for rules of use; OA articles are governed by the applicable Creative Commons License

19448007, 2022, 23, Downloaded from https://agupubs.onlinelibrary.wiley.com/doi/10.1029/2022GL100841 by University of California - Los Ange, Wiley Online Library on [09/10/2023]. See the Terms and Conditions (https://onlinelibrary.wiley.com/terms-and-conditions) on Wiley Online Library for rules of use; OA articles are governed by the applicable Creative Commons License

in northern hemisphere (Figures 4c and 4f). This is the consequence of the propagation effect mentioned in Section 3.1 where most of the wave power propagates to higher L-shells, and consequently the precipitated flux moves to higher latitudes as a function of time. The flux peak in the southern hemisphere is at a higher latitude than those on northern hemisphere, which may indicate that the cyclotron resonance responsible for microburst on southern hemisphere occurs at a higher L-shell than the anomalous cyclotron resonance responsible for the microburst in the southern hemisphere.

To describe the spatial scale size of the microburst, we define the scale size as the full width at half maximum of the precipitation flux spatial profile, as illustrated in Figure 4d. The results are plotted in the blue curves in panel (b) and (e), corresponding to the left y-axis. We see that the relativistic microburst scale size in the southern hemisphere varies between 40 and 200 km, and the scale size in the northern hemisphere varies between 10 and 45 km. This suggests that the co-streaming microbursts have a smaller scale size than the counter-streaming, cyclotron-resonance-induced microburst. Despite the wide range of scale sizes, the typical scale size of microbursts that occurs when they are strongest, is usually small. For example, when the integrated flux in the southern hemisphere reaches its maximum value at ∼0.76 s (marked by the vertical dashed black line in Figure 4e), the simultaneous scale size is at a minimum value of 40 km. For the northern hemisphere, the scale size at maximum flux is ∼20 km, as inferred from Figure 4b.

4. Discussion

We first emphasize the importance of the SP. Previous works on chorus-wave-induced microbursts all focus on the precipitation on the same field line with the chorus waves, that is, what is called the PP in this study. Recently Chen et al. (2021) and Ozaki et al. (2022) adopted a similar approach as this work and studied the precipitation signature on different L-shells. However, their L-shell range was still too close to the source L-shell, and Chen et al. didn't analyze the scale size and Ozaki et al. only focus on cyclotron resonance, so what they observed was still the PP. In this work, not only do we find the existence of the SP, but the relativistic precipitation flux contribution from SP is significant or even dominant, compared with PP.

The scale size values of 20 km (north) and 40 km (south) agree well with previous observations. This not only gives us confidence in our modeling results, but also reveals some deeper physical insights. It's important to keep in mind that the scale size we obtain should be understood as a minimum possible value due to the modeling setting up in this work. We neglect the spatial extent of chorus wave packet on the equator and simplify it as a point source, and we neglect the chirping rate of the chorus wave element and assume all waves with different frequencies are launched simultaneously at $t = 0$. This means that the chorus wave source is shrunk on both spatial and temporal extent to its minimum possible value, therefore we expect the obtained scale size to be smaller than what it is in reality. Nevertheless, our event-based modeling yields a very reasonable scale size for SP consistent with previous observations, which implies that the spatial and temporal extent of the chorus wave source might be a second order factor for SP and the scale size of the precipitation is mainly due to the wave spreading during their propagation. In contrast, there is no propagation effect involved in the formation of the PP in the equatorial source region, leading to the very short duration (several milliseconds) and the very small scale size (several km) of PP which is not realistic.

This finding provides an entirely new view than the previous assumption that the scale size of the microburst is related to the (cross-field) scale length of chorus wave elements at the equatorial (e.g., Crew et al., 2016; Shumko et al., 2018, 2020). In these works, the measured microburst scale size on the ground is mapped to the magnetic equator and compared with the chorus wave correlation length, which is claimed to be evidence that chorus waves are one possible source of microbursts. This is true for the PP but not the case in SP, where the propagation effects of chorus waves are the primary factor controlling the microburst scale size instead of the chorus wave element size, therefore allowing a point-sourced chorus wave element to produce a finite-sized microburst. As we mentioned in Section 3.1, the trajectories of chorus waves can diverge and cover a wide range of L-shell if there are multiple frequency modes and initial WNAs in the chorus element, even if the source is a point. It is this L-shell coverage that constructs the spatial distribution of microburst flux on the ground. Another piece of evidence that supports this propagation effect view is that the microburst is displaced poleward from the source L-shell of 6. This means that the major wave-particle interaction of SP does not occur at the equatorial source region (as a direct comparison of the microburst and chorus element scale size would require), but later when waves have propagated away to higher latitudes and outer L-shells. This may also raise an alarm for future

19448007, 2022, 23, Downloaded from https://agupubs.onlinelibrary.wiley.com/doi/10.1029/2022GL100841 by University of California - Los Angeles, Wiley Online Library on [09/10/2023]. See the Terms and Conditions (https://onlinelibrary.wiley.com/terms-and-conditions) on Wiley Online Library for rules of use; OA articles are governed by the applicable Creative Commons License

conjugation observation studies of microbursts suggesting that other than a rigorous field line conjugation, a low-Earth-orbit spacecraft poleward of the equatorial spacecraft might also bring new insights.

A final comment is that although the co-streaming (northern hemisphere) precipitation is only $\sim 1/3$ as strong as the counter-streaming southern one and has smaller scale size, they are still at the same order of magnitude and may not be neglected. The co-streaming anomalous cyclotron resonance is thus also an important piece of the overall precipitation picture.

5. Summary

Understanding the factors controlling the scale size of relativistic electron microbursts is a key question for understanding microburst precipitation and its impacts but has not yet fully been explored and hasn't been modeled in detail. In this work, we apply a numerical model that takes full account of the propagation effects of chorus waves in an inhomogeneous magnetosphere, and thus can obtain a global wavefield distribution induced by a single wave source and construct precipitation flux over different L-shells, leading to a microburst spatial distribution on the ground for scale size analysis. This is the first work that models the microburst spatial distribution induced by chorus waves with the inclusion of chorus wave propagation effects.

Precipitation resulting from different resonance modes is analyzed in detail. It is shown that cyclotron resonance induces strong counter-streaming relativistic precipitation, and anomalous cyclotron resonance induces co-streaming, slightly weaker relativistic precipitation. These two parts of the precipitation structure form the complete relativistic microburst. Landau resonance induces strong co-streaming sub-relativistic precipitations that may be responsible for the pulsating aurora. This part of precipitation only occurs on the co-streaming side and would not be observed in the opposite hemisphere. The (anomalous) cyclotron resonance on the source L-shell mainly occurs at lower energy level than higher L-shells, therefore only a weak high-energy tail contributes to relativistic microburst, forming the PP.

The latitudinal distribution of the relativistic microburst flux on the ground is analyzed, which is representative of both ionospheric and LEO spacecraft observations. Other than the precipitation on the wave source L-shell (PP), we also find a new kind of precipitation occurring on higher latitude and outer L-shell (SP), and its contribution to relativistic microburst is significant. SP in both hemispheres occur poleward of the chorus wave source location and continue moving poleward with time, as a result of the fact that most of the chorus wave power propagates to higher L-shells. The estimated averaged poleward displacement speed for northern and southern hemisphere microbursts are 721 and 354 km/s. Relativistic microbursts in the southern hemisphere (i.e., counter-streaming interaction) is ~ 3 time stronger than those in the north, and has a larger scale size. The relativistic microburst scale size in the northern hemisphere is $10 \sim 45\,\mathrm{km}$ and the most typical value (scale size corresponding to highest microburst flux) is $\sim 20\,\mathrm{km}$; the scale size in the southern hemisphere is $\sim 40 - 200\,\mathrm{km}$ and the most typical value is $\sim 40\,\mathrm{km}$. The typical values of microbursts are very consistent with previous observations. Such a reasonable scale size modeled by a point sourced chorus wave element indicates that the chorus waves spreading due to propagation effects can be another primary effect controlling the microburst scale size than the spatial extent of chorus wave.

Data Availability Statement

The data used in this work can be accessed from https://doi.org/10.5281/zenodo.6989822.

Acknowledgments
The authors thank the RBSP team. This work is supported by NASA FINESST award 80NSSC21K1393, NSF Geospace Environment Modeling Grant AGS-2025706, and NASA/LWS award 80NSSC21K1308.

References

Anderson, K. A., & Milton, D. W. (1964). Balloon observations of X rays in the auroral zone: 3. High time resolution studies. *Journal of Geophysical Research*, *69*(21), 4457–4479. https://doi.org/10.1029/jz069i021p04457

Artemyev, A. V., Zhang, X. J., Zou, Y., Mourenas, D., Angelopoulos, V., Vainchtein, D., et al. (2022). On the nature of intense sub-relativistic electron precipitation. *Journal of Geophysical Research: Space Physics*, *127*(6), e2022JA030571. https://doi.org/10.1029/2022ja030571

Blake, J. B., Looper, M. D., Baker, D. N., Nakamura, R., Klecker, B., & Hovestadt, D. (1996). New high temporal and spatial resolution measurements by SAMPEX of the precipitation of relativistic electrons. *Advances in Space Research*, *18*(8), 171–186. https://doi.org/10.1016/0273-1177(95)00969-8

Bortnik, J., Inan, U. S., & Bell, T. F. (2006a). Temporal signatures of radiation belt electron precipitation induced by lightning-generated MR whistler waves: 1. Methodology. *Journal of Geophysical Research*, *111*(A2), A02204. https://doi.org/10.1029/2005ja011182

Bortnik, J., Inan, U. S., & Bell, T. F. (2006b). Temporal signatures of radiation belt electron precipitation induced by lightning-generated MR whistler waves: 2. Global signatures. *Journal of Geophysical Research*, *111*(A2), A02205. https://doi.org/10.1029/2005ja011398

Breneman, A. W., Crew, A., Sample, J., Klumpar, D., Johnson, A., Agapitov, O., et al. (2017). Observations directly linking relativistic electron microbursts to whistler mode chorus: Van Allen Probes and FIREBIRD II. *Geophysical Research Letters*, *44*(22), 11–265. https://doi.org/10.1002/2017gl075001

Chen, L., Breneman, A. W., Xia, Z., & Zhang, X. J. (2020). Modeling of bouncing electron microbursts induced by ducted chorus waves. *Geophysical Research Letters*, *47*(17), e2020GL089400. https://doi.org/10.1029/2020gl089400

Chen, L., Zhang, X. J., Artemyev, A., Zheng, L., Xia, Z., Breneman, A. W., & Horne, R. B. (2021). Electron microbursts induced by nonducted chorus waves. *Frontiers in Astronomy and Space Sciences*, *8*. https://doi.org/10.3389/fspas.2021.745927

Crew, A. B., Spence, H. E., Blake, J. B., Klumpar, D. M., Larsen, B. A., O'Brien, T. P., et al. (2016). First multipoint in situ observations of electron microbursts: Initial results from the NSF FIREBIRD II mission. *Journal of Geophysical Research: Space Physics*, *121*(6), 5272–5283. https://doi.org/10.1002/2016ja022485

Douma, E., Rodger, C. J., Blum, L. W., & Clilverd, M. A. (2017). Occurrence characteristics of relativistic electron microbursts from SAMPEX observations. *Journal of Geophysical Research: Space Physics*, *122*(8), 8096–8107. https://doi.org/10.1002/2017ja024067

Douma, E., Rodger, C. J., Blum, L. W., O'Brien, T. P., Clilverd, M. A., & Blake, J. B. (2019). Characteristics of relativistic microburst intensity from SAMPEX observations. *Journal of Geophysical Research: Space Physics*, *124*(7), 5627–5640. https://doi.org/10.1029/2019ja026757

Hikishima, M., Omura, Y., & Summers, D. (2010). Microburst precipitation of energetic electrons associated with chorus wave generation. *Geophysical Research Letters*, *37*(7). https://doi.org/10.1029/2010gl042678

Hofmann, D. J., & Greene, R. A. (1972). Balloon observations of simultaneous auroral X-ray and visible bursts. *Journal of Geophysical Research*, *77*(4), 776–780. https://doi.org/10.1029/ja077i004p00776

Imhof, W. L., Voss, H. D., Mobilia, J., Datlowe, D. W., Gaines, E. E., McGlennon, J. P., & Inan, U. S. (1992). Relativistic electron microbursts. *Journal of Geophysical Research*, *97*(A9), 13829–13837. https://doi.org/10.1029/92ja01138

Johnson, M. P., Inan, U. S., & Lauben, D. S. (1999). Subionospheric VLF signatures of oblique (nonducted) whistler-induced precipitation. *Geophysical Research Letters*, *26*(23), 3569–3572. https://doi.org/10.1029/1999gl010706

Kang, N., & Bortnik, J. (2022). Structure of energy precipitation induced by superbolt-lightning generated whistler waves. *Geophysical Research Letters*, *49*(5), e2022GL097770. https://doi.org/10.1029/2022gl097770

Kawamura, M., Sakanoi, T., Fukizawa, M., Miyoshi, Y., Hosokawa, K., Tsuchiya, F., et al. (2021). Simultaneous pulsating aurora and microburst observations with ground-based fast auroral imagers and CubeSat FIREBIRD-II. *Geophysical Research Letters*, *48*(18), e2021GL094494. https://doi.org/10.1029/2021gl094494

Lauben, D. S., Inan, U. S., Bell, T. F., & Gurnett, D. A. (2002). Source characteristics of ELF/VLF chorus. *Journal of Geophysical Research*, *107*(A12), SMP-10. https://doi.org/10.1029/2000ja003019

Li, W., Thorne, R. M., Angelopoulos, V., Bortnik, J., Cully, C. M., Ni, B., et al. (2009). Global distribution of whistler-mode chorus waves observed on the THEMIS spacecraft. *Geophysical Research Letters*, *36*(9), L09104. https://doi.org/10.1029/2009gl037595

Lorentzen, K. R., Blake, J. B., Inan, U. S., & Bortnik, J. (2001). Observations of relativistic electron microbursts in association with VLF chorus. *Journal of Geophysical Research*, *106*(A4), 6017–6027. https://doi.org/10.1029/2000ja003018

Lorentzen, K. R., Looper, M. D., & Blake, J. B. (2001). Relativistic electron microbursts during the GEM storms. *Geophysical Research Letters*, *28*(13), 2573–2576. https://doi.org/10.1029/2001gl012926

Marshall, R. A., & Bortnik, J. (2018). Pitch angle dependence of energetic electron precipitation: Energy deposition, backscatter, and the bounce loss cone. *Journal of Geophysical Research: Space Physics*, *123*(3), 2412–2423. https://doi.org/10.1002/2017ja024873

Miyoshi, Y., Hosokawa, K., Kurita, S., Oyama, S. I., Ogawa, Y., Saito, S., et al. (2021). Penetration of MeV electrons into the mesosphere accompanying pulsating aurorae. *Scientific Reports*, *11*(1), 1–9. https://doi.org/10.1038/s41598-021-92611-3

Miyoshi, Y., Katoh, Y., Nishiyama, T., Sakanoi, T., Asamura, K., & Hirahara, M. (2010). Time of flight analysis of pulsating aurora electrons, considering wave-particle interactions with propagating whistler mode waves. *Journal of Geophysical Research*, *115*(A10). https://doi.org/10.1029/2009ja015127

Miyoshi, Y., Oyama, S., Saito, S., Kurita, S., Fujiwara, H., Kataoka, R., et al. (2015). Energetic electron precipitation associated with pulsating aurora: EISCAT and Van Allen Probe observations. *Journal of Geophysical Research: Space Physics*, *120*(4), 2754–2766. https://doi.org/10.1002/2014ja020690

Miyoshi, Y., Saito, S., Kurita, S., Asamura, K., Hosokawa, K., Sakanoi, T., et al. (2020). Relativistic electron microbursts as high-energy tail of pulsating aurora electrons. *Geophysical Research Letters*, *47*(21), e2020GL090360. https://doi.org/10.1029/2020gl090360

Nakamura, R., Isowa, M., Kamide, Y., Baker, D. N., Blake, J. B., & Looper, M. (2000). SAMPEX observations of precipitation bursts in the outer radiation belt. *Journal of Geophysical Research*, *105*(A7), 15875–15885. https://doi.org/10.1029/2000ja900018

O'Brien, T. P., Looper, M. D., & Blake, J. B. (2004). Quantification of relativistic electron microburst losses during the GEM storms. *Geophysical Research Letters*, *31*(4), L04802. https://doi.org/10.1029/2003gl018621

O'brien, T. P., Lorentzen, K. R., Mann, I. R., Meredith, N. P., Blake, J. B., Fennell, J. F., & Anderson, R. R. (2003). Energization of relativistic electrons in the presence of ULF power and MeV microbursts: Evidence for dual ULF and VLF acceleration. *Journal of Geophysical Research*, *108*(A8), 1329. https://doi.org/10.1029/2002ja009784

Ozaki, M., Yagitani, S., Shiokawa, K., Tanaka, Y., Ogawa, Y., Hosokawa, K., et al. (2022). Slow contraction of flash aurora induced by an isolated chorus element ranging from lower-band to upper-band frequencies in the source region. *Geophysical Research Letters*, *49*(9), e2021GL097597. https://doi.org/10.1029/2021gl097597

Parks, G. K. (1967). Spatial characteristics of auroral-zone X-ray microbursts. *Journal of Geophysical Research*, *72*(1), 215–226. https://doi.org/10.1029/jz072i001p00215

Saito, S., Miyoshi, Y., & Seki, K. (2012). Relativistic electron microbursts associated with whistler chorus rising tone elements: GEMSIS-RBW simulations. *Journal of Geophysical Research*, *117*(A10). https://doi.org/10.1029/2012ja018020

Sandahl, I., Eliasson, L., & Lundin, R. (1980). Rocket observations of precipitating electrons over a pulsating aurora. *Geophysical Research Letters*, *7*(5), 309–312. https://doi.org/10.1029/gl007i005p00309

Santolík, O., Gurnett, D. A., Pickett, J. S., Parrot, M., & Cornilleau-Wehrlin, N. (2003). Spatio-temporal structure of storm-time chorus. *Journal of Geophysical Research*, *108*(A7). 10.1029/2002JA009791

Santolík, O., Kletzing, C. A., Kurth, W. S., Hospodarsky, G. B., & Bounds, S. R. (2014). Fine structure of large-amplitude chorus wave packets. *Geophysical Research Letters*, *41*(2), 293–299. https://doi.org/10.1002/2013gl058889

Shumko, M., Gallardo-Lacourt, B., Halford, A. J., Liang, J., Blum, L. W., Donovan, E., et al. (2021). A strong correlation between relativistic electron microbursts and patchy aurora. *Geophysical Research Letters*, *48*(18), e2021GL094696. https://doi.org/10.1029/2021gl094696

19448007, 2022, 23, Downloaded from https://agupubs.onlinelibrary.wiley.com/doi/10.1029/2022GL100841 by University of California - Los Angeles, Wiley Online Library on [09/10/2023]. See the Terms and Conditions (https://onlinelibrary.wiley.com/terms-and-conditions) on Wiley Online Library for rules of use; OA articles are governed by the applicable Creative Commons License

Shumko, M., Johnson, A. T., Sample, J. G., Griffith, B. A., Turner, D. L., O'Brien, T. P., et al. (2020). Electron microburst size distribution derived with AeroCube-6. *Journal of Geophysical Research: Space Physics*, *125*(3), e2019JA027651. https://doi.org/10.1029/2019ja027651

Shumko, M., Sample, J., Johnson, A., Blake, B., Crew, A., Spence, H., et al. (2018). Microburst scale size derived from multiple bounces of a microburst simultaneously observed with the FIREBIRD-II cubeSats. *Geophysical Research Letters*, *45*(17), 8811–8818. https://doi.org/10.1029/2018gl078925

Thorne, R. M., O'Brien, T. P., Shprits, Y. Y., Summers, D., & Horne, R. B. (2005). Timescale for MeV electron microburst loss during geomagnetic storms. *Journal of Geophysical Research*, *110*(A9). https://doi.org/10.1029/2004ja010882

Tsurutani, B. T., Lakhina, G. S., & Verkhoglyadova, O. P. (2013). Energetic electron (>10 keV) microburst precipitation, ~ 5–15 s X-ray pulsations, chorus, and wave-particle interactions: A review. *Journal of Geophysical Research: Space Physics*, *118*(5), 2296–2312. https://doi.org/10.1002/jgra.50264

Zhang, X. J., Angelopoulos, V., Mourenas, D., Artemyev, A., Tsai, E., & Wilkins, C. (2022). Characteristics of electron microburst precipitation based on high-resolution ELFIN measurements. *Journal of Geophysical Research: Space Physics*, *127*(5), e2022JA030. https://doi.org/10.1029/2022ja030509

19448007, 2022, 23, Downloaded from https://agupubs.onlinelibrary.wiley.com/doi/10.1029/2022GL100841 by University of California - Los Ange, Wiley Online Library on [09/10/2023]. See the Terms and Conditions (https://onlinelibrary.wiley.com/terms-and-conditions) on Wiley Online Library for rules of use; OA articles are governed by the applicable Creative Commons License